

Article

Fabrication and Fractality of Fe₂O₃-CeO₂/ZSM-5 Composites for High-Temperature Desulfurization

Dongjing Liu ^{1,*}, Weiguo Zhou ¹ and Jiang Wu ^{2,*}¹ College of Mechanical Engineering, Tongji University, Shanghai 200092, China; tjweiguo@tongji.edu.cn² College of Energy and Mechanical Engineering, Shanghai University of Electric Power, Shanghai 200090, China* Correspondence: liudongjing19@163.com (D.L.); wujiang207@163.com (J.W.);
Tel.: +86-021-65981482 (D.L.); +86-021-35303902 (J.W.)

Received: 6 November 2017; Accepted: 8 December 2017; Published: 12 December 2017

Abstract: Fe₂O₃/ZSM-5 modified with Ce via citrate route (sol-gel approach) is applied for H₂S removal in 500–700 °C temperature range. The sulfidation activity of Fe₂O₃/ZSM-5 is appreciably promoted by introduction of Ce plausibly attributed to the synergy of Fe₂O₃ and CeO₂. 5Fe5Ce/ZSM-5 performs the optimal desulfurization behavior at 600 °C with sulfur capacity of 1020 μmol S/g, and the sulfidation process conforms to non-catalytic gas-solid redox reaction mechanism, which yields FeS₂, Ce₂S₃, and S. Fractal analysis is introduced to evaluate the surface porous structure and the adsorption capacity of the sorbent. Its surface fractal dimension is estimated by using Frenkel-Halsey-Hill (FHH) model. It considerably increases after sulfidation plausibly attributed to the formation of a few heterogeneous sulfides or elemental sulfur, which block or cover the surface pore structures of sorbents.

Keywords: desulfurization; fractal analysis; zeolite; cerium oxide; iron oxide

1. Introduction

Gasification and gasification-integrated energy conversion system, such as Integrated Coal Gasification Combined Cycle (IGCC) power generation system, has been considered as one of the most potential clean coal technologies in 21st century. It can greatly enhance the power generation efficiency and lower the pollutant emissions causing environmental pollution [1–3]. In an IGCC power plant, hot coal gas containing amounts of sulfur compounds is first purified and then introduced into gas turbines for generating electricity. H₂S is the major sulfur compound in the hot coal gas and it needs to be eliminated before utilization for the sake of protecting the turbine leaves from corrosion and guarantying the lower sulfur emission [4,5]. Therefore, high-temperature desulfurizer plays a crucial role in IGCC technology.

Many metal oxides have been applied for high-temperature desulfurization, such as, ZnO [6,7], CuO [8,9], MnO_x [10,11], and CeO₂ [12–14]. However, iron oxide is the most widely used sorbent for hot coal gas desulfurization in the field of the coal chemical industry owing to its good adsorption capacity, abundant resource, lower cost, and good physical strength [15–19]. Doping cerium ion (Ce⁴⁺) into Fe₂O₃ lattice can generate more oxygen vacancies which facilitate the activation and transport of the oxygen species. The generated surface oxygen vacancies and bulk oxygen species with relatively high mobility are favorable for sulfur removal [20]. However, unsupported sorbents often suffer from sintering and low mechanical strength, thus, Fe₂O₃-CeO₂ mixed oxides are deposited onto ZSM-5 with a good surface area and pore structures to alleviate these problems.

The Fe₂O₃-CeO₂/ZSM-5 sorbents with various Fe/Ce molar ratios are fabricated via citrate route and characterized by nitrogen adsorption-desorption isotherms, scanning electron microscope (SEM), X-ray diffraction (XRD) techniques, and hydrogen temperature programmed reduction (H₂-TPR). The H₂S adsorption tests are performed to study the effects of reaction temperature and CeO₂ content

on the desulfurization performance of Fe_2O_3 -based sorbents, and the process of H_2S adsorption on Fe_2O_3 - CeO_2 /ZSM-5 are then discussed. To obtain a better understanding of the textural structure or surface characteristics of the sorbent, fractal analysis is employed to address the changes in sorbent fractality or surface fractal dimension before and after sulfidation reaction, which aims to enrich the knowledge about the fractal nature of Fe_2O_3 -based sorbents.

2. Results and Discussion

2.1. Characterization Analysis

The SEM images of ZSM-5, fresh and spent 5Fe5Ce/ZSM-5 are presented in Figure 1. ZSM-5 comprises of a few rectangular granules with smooth and angular surface (Figure 1a,b). The rectangular ZSM-5 particles can be observed in fresh and spent sorbents as well, and the teeny particles on ZSM-5 surface in fresh 5Fe5Ce/ZSM-5 are likely assigned to the active phases of cerium oxides and iron oxides (Figure 1c). After sulfidation, amounts of porous aggregates related to sulfides or elemental sulfur are detected in the spent 5Fe5Ce/ZSM-5 (Figure 1d).

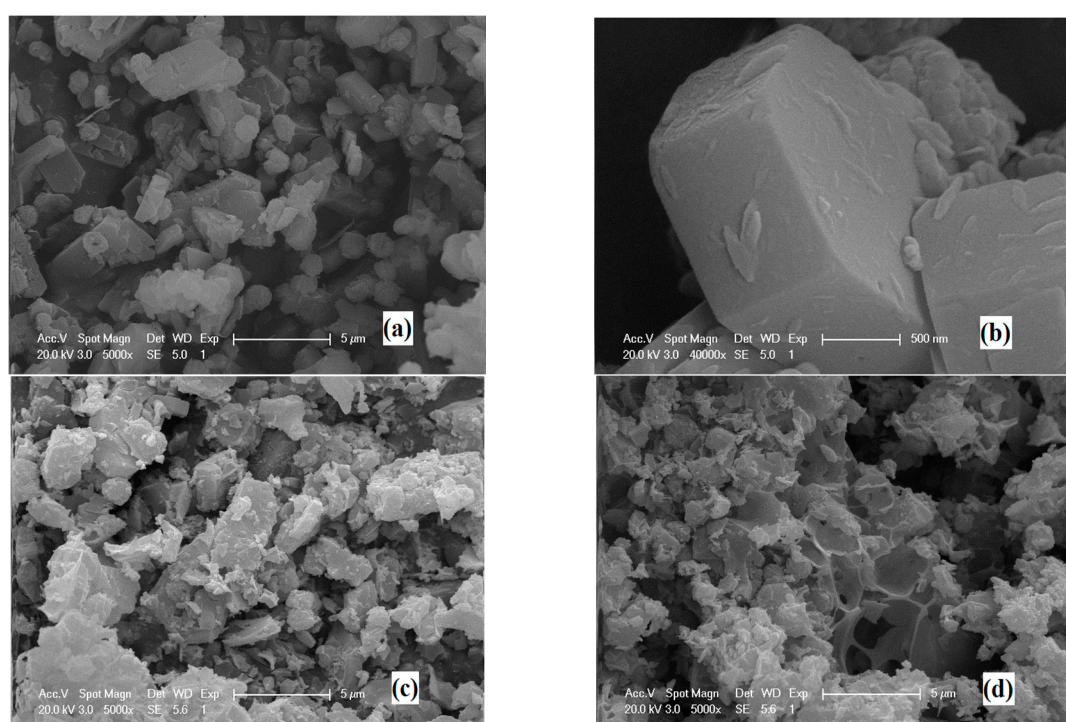


Figure 1. Scanning electron microscopy (SEM) images: (a,b) ZSM-5; (c) fresh 5Fe5Ce/ZSM-5; (d) spent 5Fe5Ce/ZSM-5 ($600\text{ }^\circ\text{C}$, $30,000\text{ mL}\cdot\text{h}^{-1}\cdot\text{g}^{-1}$, $0.2\%\text{ H}_2\text{S}/\text{N}_2$).

The sorbent textural features are examined using nitrogen adsorption-desorption techniques, ZSM-5, fresh and spent 5Fe5Ce/ZSM-5 all show typical feature of Type I nitrogen adsorption isotherm (Figure 2a), indicating that micropore structures present in the ZSM-5 and the sorbents. However, the nitrogen uptake decreases after calcination and desulfurization processes, probably because that the active metal oxides and the sulfidation products may block or cover the pore structures on ZSM-5 surface, which can be further verified from the decrease in volume values of $\sim 3.89\text{ nm}$ pore structures (Figure 2b). The surface area and total pore volume of ZSM-5 are $320\text{ m}^2/\text{g}$ and $255\text{ mm}^3/\text{g}$ respectively, the surface area decreases to 170 and $116\text{ m}^2/\text{g}$, the total pore volume reduces to 119 and $78\text{ mm}^3/\text{g}$ after calcination and sulfidation processes relatively (Table 1). However, the average pore diameter slightly diminishes from 3.19 nm to 2.79 and 2.69 nm correspondingly.

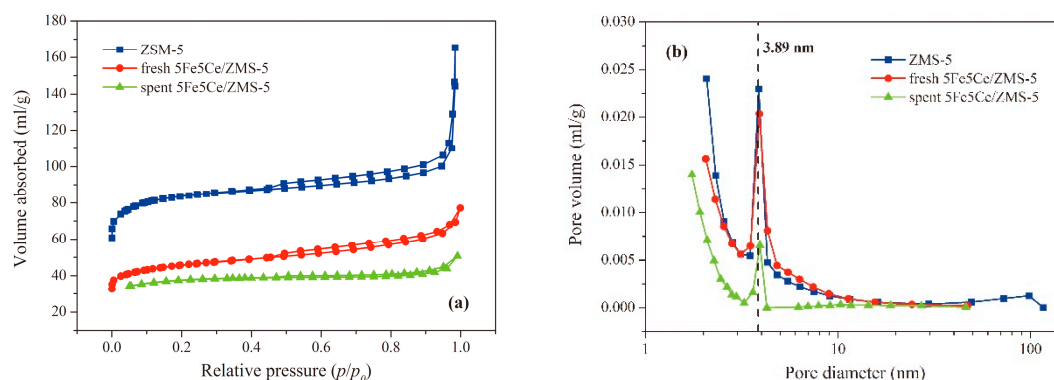


Figure 2. Textural properties of 5Fe5Ce/ZSM-5: (a) nitrogen adsorption-desorption isotherms and (b) pore size distribution.

Table 1. Brunauer-Emmett-Teller (BET) specific surface area (S_{BET}), total pore volume (V_{total}), micropore volume (V_{micro}), mesopore volume (V_{meso}), average pore diameter (D_{aver}) of ZSM-5, fresh and spent 5Fe5Ce/ZSM-5.

Sample	S_{BET}	V_{total}	V_{micro}	V_{meso}	D_{aver}
	m^2/g	mm^3/g	mm^3/g	mm^3/g	nm
ZSM-5	320	255	108	147	3.19
fresh 5Fe5Ce/ZSM-5	170	119	59	60	2.79
spent 5Fe5Ce/ZSM-5	116	78	43	35	2.69

The XRD profiles of ZSM-5, fresh and spent sorbents are shown in Figure 3, ZSM-5 presents a conspicuous diffraction peak at $2\theta = \sim 23^\circ$, it can be clearly observed in fresh and spent sorbents, and its intensity only slightly reduce after preparation and sulfidation processes (Figure 3a), suggesting that it has a good thermal stability. The diffraction signals at $2\theta = 32.8^\circ, 35.5^\circ, 40.2^\circ, 49.3^\circ, 53.9^\circ,$ and 62.2° are ascribed to Fe_2O_3 [PDF#65-7467]. The specific peaks at $2\theta = 28.5^\circ, 33.1^\circ, 47.7^\circ, 56.4^\circ, 59.1^\circ, 69.3^\circ, 76.8^\circ,$ and 78.9° are related to CeO_2 [PDF#34-0394]. The intensity of Fe_2O_3 peak gradually decreases with the increase of Ce molar fraction plausibly attributed to the strong interaction between Fe_2O_3 and CeO_2 , suggesting that metal oxides disperse well on ZSM-5 surface. For the spent 5Fe5Ce/ZSM-5, the signals at $2\theta = 28.5^\circ, 32.8^\circ, 59.4^\circ$ are assigned to FeS_2 [PDF#65-3321], the peaks at $2\theta = 31.7^\circ,$ and 37.2° are related to Ce_2S_3 [PDF#21-0189], and the diffraction signals of S [PDF#08-0247] at $2\theta = 26.5^\circ, 43.3^\circ, 51.3^\circ, 57.3^\circ, 66.7^\circ,$ and 69.0° are detected as well (Figure 3b). Thus, sulfidation of 5Fe5Ce/ZSM-5 yields $FeS_2, Ce_2S_3,$ and S. The crystalline sizes of the pristine ZSM-5 and the ZSM-5 loaded with metal oxides are estimated from the calculation of its (3 3 0) lattice plane, the crystalline size of the pristine ZSM-5 is 56 nm, which slightly decreases after loading metal oxides and sulfidation reaction. With rising CeO_2 doping ratios, the Fe_2O_3 peaks of fresh $xFe_yCe/ZSM-5$ generally shift towards higher diffraction angles, plausibly suggesting the expansion of Fe_2O_3 lattice, the crystalline sizes of Fe_2O_3 estimated from the calculation of its (1 1 0) lattice plane range from 18 to 65 nm, while the CeO_2 peaks of fresh $xFe_yCe/ZSM-5$ generally shift toward lower diffraction angles, probably indicating the contraction of CeO_2 lattice. The crystalline size of CeO_2 in fresh 5Fe5Ce/ZSM-5 estimated from the calculation of its (1 1 1) lattice plane is 21.12 nm, it appreciably increases to 24.99 nm due to the formation of Ce_2S_3 product after sulfidation, which suggests that the CeO_2 crystalline grains in fresh 5Fe5Ce/ZSM-5 probably aggregate during high-temperature desulfurization.

The H_2 -TPR profiles of $xFe_yCe/ZSM-5$ sorbents are shown in Figure 4, the adsorption peaks at 352–387 °C are related to the reduction of Fe_2O_3 to Fe_4O_3 , then Fe_4O_3 will be reduced to FeO at high temperature of 534–605 °C [21]. The major reduction peaks slightly shift towards lower temperature with increasing CeO_2 adding amount from 10 at. % to 50 at. %, which indicates that doping CeO_2 into

Fe_2O_3 lattice can improve the sorbent reducibility. However, the reduction peaks obviously shift to a higher temperature when CeO_2 molar fraction exceeds 50 at. %, which suggests that excessive CeO_2 would inhibit the reduction of the sorbent.

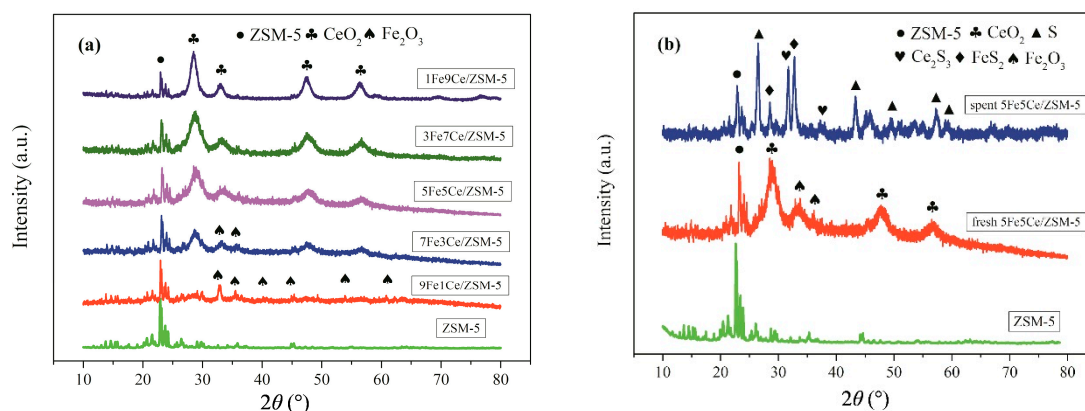


Figure 3. X-ray diffraction (XRD) patterns: (a) ZSM-5 and fresh $x\text{Fe}/\text{Ce}/\text{ZSM-5}$; (b) fresh and spent 5Fe5Ce/ZSM-5.

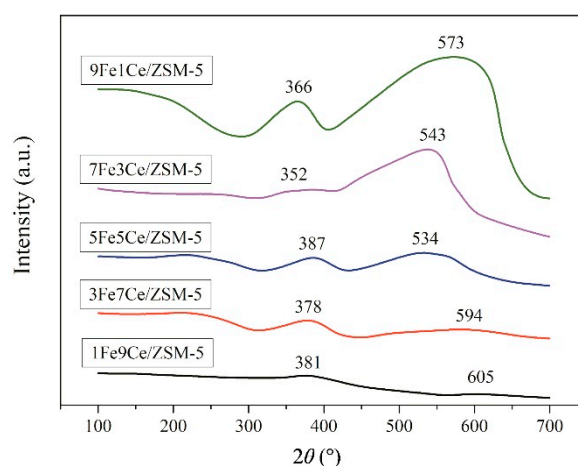


Figure 4. H_2 -TPR profiles of $x\text{Fe}/\text{Ce}/\text{ZSM-5}$.

2.2. Effect of Reaction Temperature

The breakthrough time of 5Fe5Ce/ZSM-5 first increases and then decreases with the elevation of reaction temperature (Figure 5a). 5Fe5Ce/ZSM-5 offers a good H_2S removal ability at 600 °C. 5Fe5Ce/ZSM-5 performs the greatest sulfur capacity of 1020 $\mu\text{mol S/g}$ and the longest breakthrough time of 20 min. The H_2S reaction rate with metal oxides and the H_2S diffusion rate can be promoted by increasing the reaction temperatures, the breakthrough time of 5 min and sulfur capacity of 408 $\mu\text{mol S/g}$ over 5Fe5Ce/ZSM-5 at 500 °C are very low by the reason of lower H_2S diffusion rate, and only the metal oxides on the sorbent surface react (Figure 5b). When the reaction temperature increases from 600 to 700 °C, the breakthrough time and sulfur capacity drop from 20 min and 1020 $\mu\text{mol S/g}$ to 10 min and 408 $\mu\text{mol S/g}$ correspondingly, and the breakthrough curve becomes flatter with lower slope, possibly due to the limitation of H_2S diffusion for the reason that some active phases sinter or aggregate at 700 °C. Thus, the optimum temperature of sulfidation process is 600 °C [22,23].

2.3. Effect of CeO₂ Content

The H₂S breakthrough curves and sulfur capacities of ZSM-5 and different sorbents are depicted in Figure 6, ZSM-5 is almost immediately broken through with sulfur capacity of nearly zero, suggesting that ZSM-5 is inert to hydrogen sulfide. The pure CeO₂ and Fe₂O₃ present fairly poor desulfurization performances with short breakthrough time of ~5 min and lower sulfur capacity of ~400 μmol S/g. The breakthrough time of Fe₂O₃-based sorbents is only 5–10 min by addition of 10–30 at. % CeO₂, it suddenly increases to 20 min with CeO₂ molar fraction rising to 50 at. %. However, the breakthrough time and sulfur capacity slightly decrease to 15 min and 816 μmol S/g respectively with further addition of CeO₂, possibly because some CeO₂ crystals dissolve out. The 5Fe5Ce/ZSM-5 (doping 50 at. % CeO₂) performs the longest breakthrough time of 20 min and the greatest sulfur capacity of 1020 μmol S/g, plausibly due to the intimate mixing of Fe₂O₃ and CeO₂.

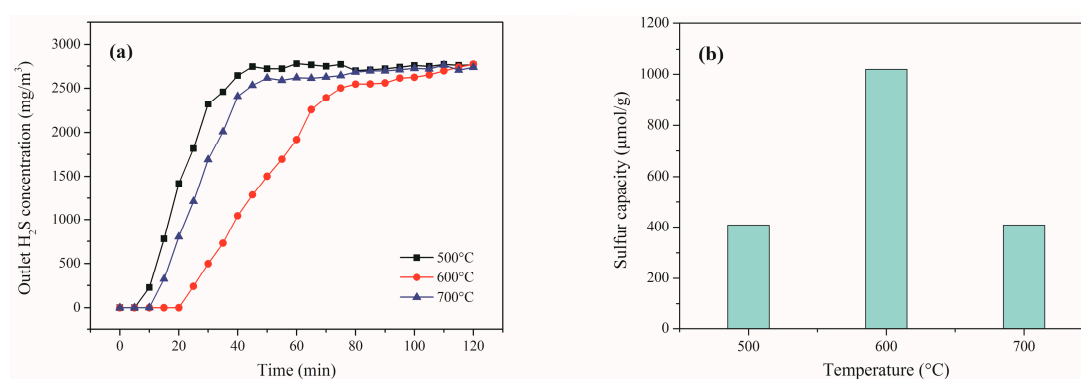


Figure 5. (a) H₂S breakthrough curves and (b) sulfur capacities of 5Fe5Ce/ZSM-5 at different temperatures (30,000 mL·h⁻¹·g⁻¹; 0.2% H₂S/N₂).

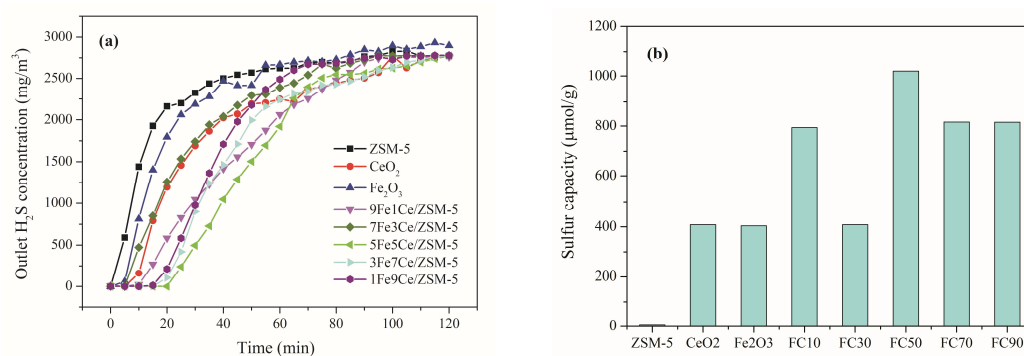


Figure 6. (a) H₂S breakthrough curves and (b) sulfur capacities of xFeyCe/ZSM-5 with various CeO₂ contents (600 °C; 30,000 mL·h⁻¹·g⁻¹; 0.2% H₂S/N₂).

2.4. Reusability

The H₂S breakthrough curves and sulfur capacities of three successive desulfurization and regeneration (regenerated by 5% O₂/N₂ mixture) cycles over 5Fe5Ce/ZSM-5 at identical temperature of 600 °C and gas flow rate of 30,000 mL·h⁻¹·g⁻¹ are presented in Figure 7. The desulfurization performance reduces a little bit after the first cycle, and the sulfur capacity decreases from 1020 μmol S/g to 816 μmol S/g, plausibly because the active phases (Fe₂O₃ and CeO₂) aggregate or sinter during the high-temperature sulfidation and regeneration processes. However, the sulfur capacity nearly does not change after the second cycle and stays at ~800 μmol S/g.

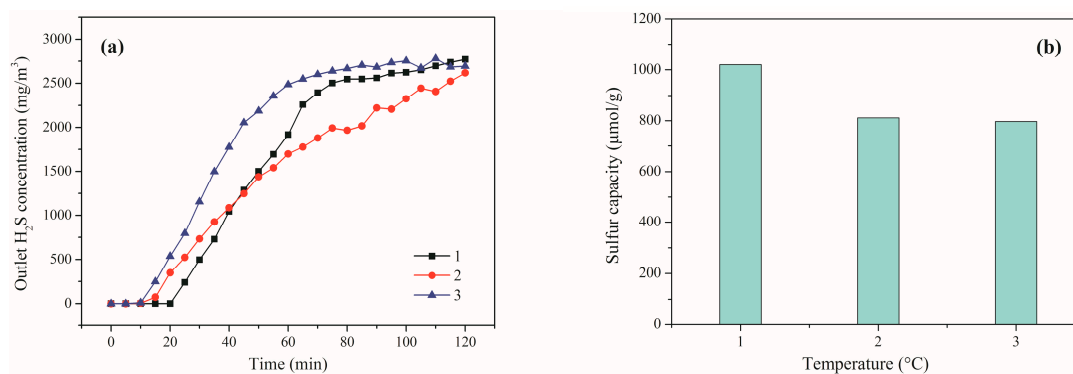


Figure 7. (a) H₂S breakthrough curves and (b) sulfur capacities of 3 successive desulfurization and regeneration cycles over 5Fe5Ce/ZSM-5 (desulfurization: 600 °C; 30,000 mL·h⁻¹·g⁻¹; 0.2% H₂S/N₂; regeneration: 600 °C; 30,000 mL·h⁻¹·g⁻¹; 5% O₂/N₂).

3. Experimental

3.1. Sorbent Preparation

The Fe₂O₃-based sorbents are prepared by using sol-gel approach which has been described in our previous paper [24,25]. Typically, stoichiometric amounts of ferric nitrate Fe(NO₃)₃·9H₂O and cerous nitrate Ce(NO₃)₃·6H₂O are dissolved in 25 mL of nitric acid (~2 mol/L). After addition of citric acid with a mole amount of 1.5 times that of the total metal ions, H-ZSM-5 (the content of active components (CeO₂ + Fe₂O₃) with respect to ZSM-5 is 50 wt. %, the Si/Al ratio of the pristine ZSM-5 is 31.65:1 [24], Tianjin, Catalyst Plant of Nankai University) is added to the solution. The mixtures are kept at 60 °C over a water bath until viscous gels form. Then, the gels firstly age at ambient temperature for 3 days, dry at 120 °C for 12 h, and finally calcine at 600 °C for 6 h in a muffle furnace [26]. The pure CeO₂ and Fe₂O₃ are prepared via the same procedure without adding ZSM-5. Fe₂O₃-based sorbents with a specific Ce molar fraction of 10, 30, 50, 70, and 90 at. % are denoted as 9Fe1Ce/ZSM-5 (or FC10), 7Fe3Ce/ZSM-5 (or FC30), 5Fe5Ce/ZSM-5 (or FC50), 3Fe7Ce/ZSM-5 (or FC70), and 1Fe9Ce/ZSM-5 (or FC90), respectively. The spent 5Fe5Ce/ZSM-5 sample is obtained from sulfidation at 600 °C, 30,000 mL·h⁻¹·g⁻¹, and 0.2% H₂S/N₂.

3.2. Sorbent Characterization

The surface micro-morphologies of ZSM-5, fresh and spent sorbents are measured using field emission scanning electron microscopy (Phillips XL-30 FEG/NEW, Eindhoven, The Netherlands), their textural properties are determined via nitrogen adsorption-desorption isotherm (Micromeritics ASAP 2020, Norcross, GA, USA), and their pore size distributions are obtained from Barrett-Joyner-Halenda (BJH) formula using the desorption branch of nitrogen isotherm. XRD patterns are attained on an X-ray diffractometer (Bruker D8 Advance, Karlsruhe, Germany), the crystalline sizes are estimated from Debye-Scherrer formula, and redox properties are examined via H₂-TPR (ChemiSorb 2720 chemisorption analyzer from Micromeritics Instrument Corp., Norcross, GA, USA), the specimens are heated from room temperature to 700 °C in a 10% H₂/Ar mixture with a flow rate of 40 mL/min at a rate of 10 °C/min.

3.3. Adsorption

H₂S adsorption tests are carried out in a vertical fixed-bed microreactor loaded with 0.2 g sorbents [27,28], the H₂S breakthrough concentration is determined as 50 mg/m³. The flow rate (30,000 mL·h⁻¹·g⁻¹) of feeding gas (0.2% H₂S/N₂ mixture) are precisely controlled by mass flow controllers. The sorbents are firstly heated up to the desired reaction temperature in N₂ to remove the impurities adsorbed on the sorbent surface prior to hydrogen sulfide adsorption. After sulfidation tests,

pure N₂ purges the desulfurization system until the sorbent bed cools down to ambient temperature. The H₂S concentration of the outlet gas is measured by a gas chromatograph (Fuli Analytical Instrument Co., Ltd., GC9790IIIH-2, Taizhou, China). The breakthrough time is defined as the duration before the breakthrough point, and the breakthrough sulfur capacity is calculated by following formula

$$S_{cap} = \frac{W_m}{V_m} \times \left[\int_0^t (C_{in} - C_{out}) dt \right] \quad (1)$$

here S_{cap} denotes the breakthrough sulfur capacity ($\mu\text{mol S/g}$), W_m is the weight hourly space velocity ($\text{L}\cdot\text{h}^{-1}\cdot\text{g}^{-1}$), V_m means molar volume of H₂S at 1 atm and 25 °C (24.5 L/mol), t stands for the breakthrough time (h), C_{in} and C_{out} denote the inlet and outlet H₂S concentration (ppm_v), respectively.

4. Desulfurization Process

According to the XRD analysis, it can be concluded that the sulfidation of 5Fe5Ce/ZSM-5 yields metal sulfides (Ce₂S₃ and FeS₂) and elemental sulfur (S). It follows typical non-catalytic gas-solid redox reaction. The sulfidation reaction can be described with the shrinking core model [29,30]. The sulfidation process mainly occurs at the sorbent surface, and the sorbent particles consist of unreacted core and reacted outside product layers. The unreacted core gradually shrinks, but the product layer gradually grows until the whole sorbent particle consumes. The schematic diagram of the sulfidation process is shown in Figure 8, which incorporates five consecutive processes: (1) gaseous H₂S(g) diffusing from gas bulk onto the sorbent surface forms adsorbed state H₂S(ad), (2) the H₂S(ad) penetrates through the newly formed product layer to the surface of the unreacted core, (3) the H₂S(ad) reacts with the active metal oxides of the sorbent, (4) sulfidation products (metal sulfides and elemental sulfur) form new product layer and the reaction product H₂O(g) penetrates through the product layer to the external surface of the sorbent, and (5) the H₂O(g) continues to diffuse from sorbent external surface to the gas bulk [31,32].

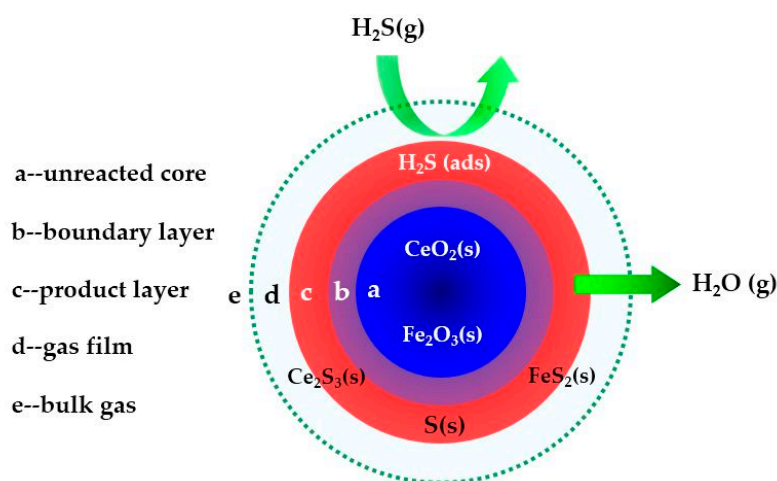


Figure 8. Schematic diagram of sulfidation process.

5. Fractal Analysis

In recent decades, fractal analysis has been widely applied in a few fields of scientific researches to characterize the geometric and structural properties of fractal surfaces and pore structures [33,34]. Fractal dimension is often adopted to quantitatively evaluate the irregularities of the fractal surface and pore structures. Its value varies from 2 to 3, in which the lowest value 2 corresponds to a perfectly regular smooth surface, while the upper limit 3 regards to the maximum allowed complexity of the irregular or rough surface [35]. To date, many studies have revealed that surface fractality plays an important role in physicochemical processes such as diffusion, reaction kinetics,

and adsorption [36], and the fractal concept can be adopted to elucidate the relationship between the adsorption performance and the surface structure of the sorbents.

One of the simplest and most popular relationships for determining the surface fractal dimension (D_s) of a solid by using adsorption isotherm data is the Frenkel-Halsey-Hill equation (FHH) [37,38], which in logarithmic form can be expressed as follows:

$$\ln\left(\frac{V}{V_m}\right) = C + A \cdot \ln\left(\ln\left(\frac{P_0}{P}\right)\right) \quad (2)$$

where V is the nitrogen uptake at equilibrium pressure P , V_m is the nitrogen uptake of a monolayer coverage, P_0 is the saturation pressure, A is a power-law exponent dependent on the surface fractal dimension and the adsorption mechanism, and C is a pre-exponential factor. Two limiting adsorption forces are considered: one is van der Waals at the early stages of adsorption, and the other is capillary condensation (surface tension) at later stages. At the early stage of adsorption, the van der Waals forces between gas-solid interactions are dominant and the gas-liquid surface tension forces are negligibly small. Then, the relationship between A and D_s can be derived as follows

$$D_s = 3(1 + A) \quad (3)$$

However, for higher coverages at the later stage of adsorption, the interface is controlled by gas-liquid surface tension forces and the relationship between A and D_s changes to the following expression

$$D_s = 3 + A \quad (4)$$

The nitrogen uptake of the monolayer coverage can be obtained by using Brunauer-Emmett-Teller (BET) surface area calculation formula as follows

$$\frac{1}{V\left(\frac{P_0}{P} - 1\right)} = \frac{1}{cV_m} + \frac{c-1}{cV_m} \frac{P}{P_0} \quad (5)$$

where P/P_0 is the relative pressure and c is a constant.

Plot $1/[V(P/P_0 - 1)]$ versus P/P_0 , and linearly fits it in the P/P_0 range of 0.05–0.35 (Figures 9a and 10a), the slope of the fitting curve is equal to $(c - 1)/(cV_m)$, and the intercept of the fitting curve is equal to $1/cV_m$. Thus, the value of V_m can be determined according to the slope and intercept of the fitting curve. Then, a plot of $\ln(V/V_m)$ versus $\ln(\ln(P/P_0))$ fitting by using least-square method will show a linear trend (Figures 9b and 10b) as well, and the slope of the fitting line is equal to A , which can be used for calculating the value of the surface fractal dimension according to Equation (3). The surface fractal dimension of the fresh 5Fe5Ce/ZSM-5 is 2.61, and it considerably increases to 2.96 after the sulfidation reaction, which indicates a more sophisticated pore distribution for the spent 5Fe5Ce/ZSM-5, and the higher value suggests that the surfaces of the spent 5Fe5Ce/ZSM-5 is more irregular [39].

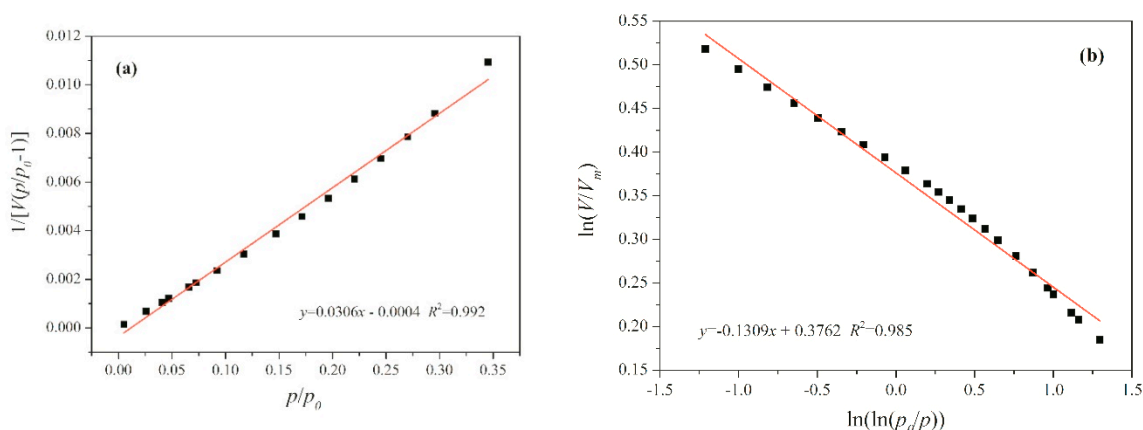


Figure 9. Fractal analysis of fresh 5Fe5Ce/ZSM-5: (a) fitting curve for nitrogen uptake of a monolayer coverage and (b) fitting curve for surface fractal dimension.

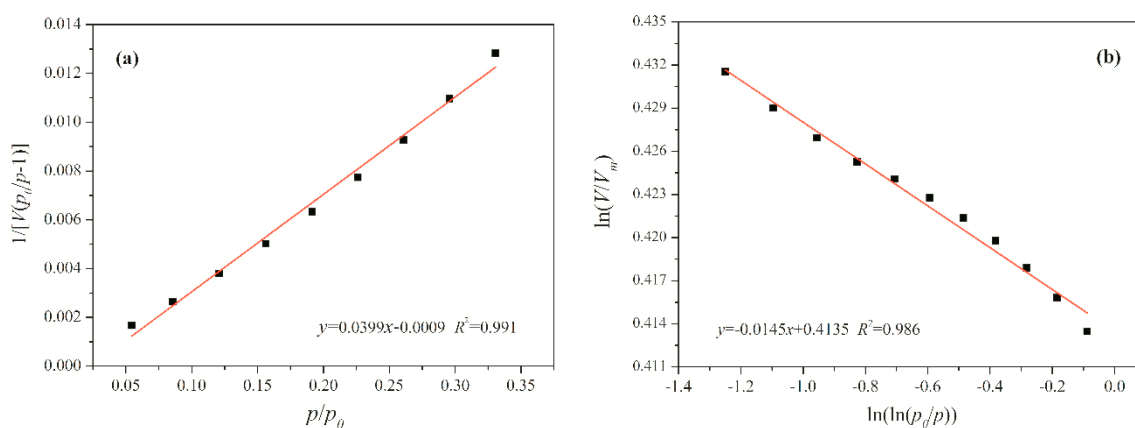


Figure 10. Fractal analysis of spent 5Fe5Ce/ZSM-5: (a) fitting curve for nitrogen uptake of a monolayer coverage and (b) fitting curve for surface fractal dimension.

6. Conclusions

The $\text{Fe}_2\text{O}_3/\text{ZSM-5}$ composites modified with CeO_2 are synthesized for H_2S removal in the temperature range of 500–700 °C. The XRD and H_2 -TPR results show that the reducibility of $\text{Fe}_2\text{O}_3/\text{ZSM-5}$ is promoted by adding appropriate amounts of CeO_2 , and $\text{Fe}_2\text{O}_3/\text{ZSM-5}$ composites perform better by incorporating 30–50 at. % Ce^{4+} ions into Fe_2O_3 lattices attributed to the cooperative effect of Fe_2O_3 and CeO_2 . The optimal sulfur capacity of 1020 $\mu\text{mol S/g}$ over 5Fe5Ce/ZSM-5 is achieved at 600 °C, and the sulfidation process is in agreement with non-catalytic gas-solid redox reaction mechanism. The surface textural properties and the pore structures of the fresh and spent 5Fe5Ce/ZSM-5 sorbent is studied in the fractal theory point of view. The surface fractal dimension of 5Fe5Ce/ZSM-5 increases from 2.61 to 2.96 after sulfidation reaction probably attributed to the formation of numerous micropore structures of highly complexity and irregularity.

Acknowledgments: This work was partially sponsored by Natural Science Foundation of China (21237003, 50806041) and Shanghai Science and Technology Commission (12dz1201702, 15dz1200703, 15110501000).

Author Contributions: Dongjing Liu conducted the experiments and wrote the paper; Weiguo Zhou and Jiang Wu contributed valuable ideas and discussions.

Conflicts of Interest: The authors declare no conflict of interest.

References

1. Huang, Y.; Rezvani, S.; McIlveen-Wright, D.; Minchener, A.; Hewitt, N. Techno-economic study of CO₂ capture and storage in coal fired oxygen fed entrained flow IGCC power plants. *Fuel Process. Technol.* **2008**, *89*, 916–925. [[CrossRef](#)]
2. Dutta, A.; Cheah, S.; Bain, R.; Feik, C.; Magrini-Bar, K.; Phillips, S. Integrated process configuration for high-temperature sulfur mitigation during biomass conversion via indirect gasification. *Ind. Eng. Chem. Res.* **2012**, *51*, 8326–8333. [[CrossRef](#)]
3. Higman, C.; Tam, S. Advances in coal gasification, hydrogenation, and gas treating for the production of chemicals and fuels. *Chem. Rev.* **2014**, *114*, 1673–1708. [[CrossRef](#)] [[PubMed](#)]
4. Liu, H.W.; Ni, W.D.; Li, Z.; Ma, L.W. Strategic thinking on IGCC development in China. *Energy Policy* **2008**, *36*, 1–11. [[CrossRef](#)]
5. Giuffrida, A.; Romano, M.C.; Lozza, G.C. Thermodynamic assessment of IGCC power plants with hot fuel gas desulfurization. *Appl. Energy* **2010**, *87*, 3374–3383. [[CrossRef](#)]
6. Bu, X.P.; Ying, Y.J.; Zhang, C.Q.; Peng, W.W. Research improvement in Zn-based sorbent for hot gas desulfurization. *Powder Technol.* **2008**, *180*, 253–258. [[CrossRef](#)]
7. Pineda, M.; Palacios, J.M.; Alonso, L.; García, E.; Moliner, R. Performance of zinc oxide based sorbents for hot coal gas desulfurization in multicycle tests in a fixed-bed reactor. *Fuel* **2000**, *79*, 885–895. [[CrossRef](#)]
8. Karvana, O.; Atakül, H. Investigation of CuO/mesoporous SBA-15 sorbents for hot gas desulfurization. *Fuel Process. Technol.* **2008**, *89*, 908–915. [[CrossRef](#)]
9. Karvana, O.; Sirkecioğlu, A.; Atakül, H. Investigation of nano-CuO/mesoporous SiO₂ materials as hot gas desulphurization sorbents. *Fuel Process. Technol.* **2009**, *90*, 1452–1458. [[CrossRef](#)]
10. Wang, J.; Liang, B.; Parnas, R. Manganese-based regenerable sorbents for high temperature H₂S removal. *Fuel* **2013**, *107*, 539–546. [[CrossRef](#)]
11. Bakker, W.J.W.; Kapteijn, F.; Moulijn, J.A. A high capacity manganese-based sorbent for regenerative high temperature desulfurization with direct sulfur production conceptual process application to coal gas cleaning. *Chem. Eng. J.* **2003**, *96*, 223–235. [[CrossRef](#)]
12. Dooley, K.M.; Kalakota, V.; Adusumilli, S. High-temperature desulfurization of gasifier effluents with rare earth and rare earth transition metal oxides. *Energy Fuels* **2011**, *25*, 1213–1220. [[CrossRef](#)]
13. Li, R.; Krcha, M.D.; Janik, M.J.; Roy, A.D.; Dooley, K.M. Ce-Mn oxides for high-temperature gasifier effluent desulfurization. *Energy Fuels* **2012**, *26*, 6765–6776. [[CrossRef](#)]
14. Yasyerli, S.; Dogu, G.; Dogu, T. Selective oxidation of H₂S to elemental sulfur over Ce-V mixed oxide and CeO₂ catalysts prepared by the complexation technique. *Catal. Today* **2006**, *1–3*, 271–278. [[CrossRef](#)]
15. Pan, Y.G.; Perales, J.F.; Velo, E.; Puigjaner, L. Kinetic behaviour of iron oxide sorbent in hot gas desulfurization. *Fuel* **2005**, *84*, 1105–1109. [[CrossRef](#)]
16. Xie, W.; Chang, L.P.; Wang, D.H.; Xie, K.C.; Wall, T.; Yu, J.L. Removal of sulfur at high temperatures using iron-based sorbents supported on fine coal ash. *Fuel* **2010**, *89*, 868–873. [[CrossRef](#)]
17. White, J.D.; Groves, F.R., Jr.; Harrison, D.P. Elemental sulfur production during the regeneration of iron oxide high-temperature desulfurization sorbent. *Catal. Today* **1998**, *40*, 47–57. [[CrossRef](#)]
18. Fan, H.L.; Sun, T.; Zhao, Y.P.; Shangguan, J.; Lin, J.Y. Three-dimensionally ordered macroporous iron oxide for removal of H₂S at medium temperatures. *Environ. Sci. Technol.* **2013**, *47*, 4859–4865. [[CrossRef](#)] [[PubMed](#)]
19. Li, P.; Xin, Y.; Li, Q.; Wang, Z.P.; Zhang, Z.L.; Zheng, L.R. Ce-Ti amorphous oxides for selective catalytic reduction of NO with NH₃: Confirmation of Ce-O-Ti active sites. *Environ. Sci. Technol.* **2012**, *17*, 9600–9605. [[CrossRef](#)] [[PubMed](#)]
20. Zhu, F.; Li, C.; Fan, H. Effect of binder on the properties of iron oxide sorbent for hot gas desulfurization. *J. Nat. Gas Chem.* **2010**, *19*, 169–172. [[CrossRef](#)]
21. Chen, K.; Fan, Y.; Hu, Z.; Yan, Q. Study on the Reduction Behavior of zirconia supported iron oxide catalysts by temperature-programmed reduction combined with in situ mössbauer spectroscopy. *J. Solid State Chem.* **1996**, *121*, 240–246. [[CrossRef](#)]
22. Zhang, Z.F.; Liu, B.S.; Wang, F.; Li, J.F. Fabrication and performance of xMnyCe/hexagonal mesoporous silica sorbents with wormhole-like framework for hot coal gas desulfurization. *Energy Fuels* **2013**, *27*, 7754–7761. [[CrossRef](#)]

23. Liu, D.J.; Zhou, W.G.; Wu, J. CuO-CeO₂/ZSM-5 composites for reactive adsorption of hydrogen sulfide at high temperature. *Can. J. Chem. Eng.* **2016**, *94*, 2276–2281. [[CrossRef](#)]
24. Liu, D.J.; Zhou, W.G.; Wu, J. CeO₂-MnO_x/ZSM-5 sorbents for H₂S removal at high temperature. *Chem. Eng. J.* **2016**, *284*, 862–871. [[CrossRef](#)]
25. Liu, D.J.; Zhou, W.G.; Wu, J. CeO₂-La₂O₃/ZSM-5 sorbents for high-temperature H₂S removal. *Korean J. Chem. Eng.* **2016**, *33*, 1837–1845. [[CrossRef](#)]
26. Liu, B.S.; Wan, Z.Y.; Zhan, Y.P.; Au, C.T. Desulfurization of hot coal gas over high-surface-area LaMeO_x/MCM-41 sorbents. *Fuel* **2012**, *98*, 95–102. [[CrossRef](#)]
27. Liu, D.J.; Zhou, W.G.; Wu, J. Perovskite LaMnO₃/ZSM-5 composites for H₂S reactive adsorption at high temperature. *Adsorption* **2016**, *22*, 327–334. [[CrossRef](#)]
28. Liu, D.J.; Zhou, W.G.; Wu, J. La₂CuO₄/ZSM-5 sorbents for high-temperature desulphurization. *Fuel* **2016**, *177*, 251–259. [[CrossRef](#)]
29. Neveux, L.; Chiche, D.; Pérez-Pellitero, J.; Favergeon, L.; Gay, A.S.; Pijolat, M. New insight into the ZnO sulfidation reaction: Mechanism and kinetics modeling of the ZnS outward growth. *Phys. Chem. Chem. Phys.* **2013**, *15*, 1532–1545. [[CrossRef](#)] [[PubMed](#)]
30. Chiche, D.; Bazer, D. New insight on the ZnO sulfidation reaction: Evidences for an outward growth process of the ZnS phase. *Chem. Eng. J.* **2012**, *181–182*, 508–515.
31. Liu, D.J.; Zhou, W.G.; Wu, J. Effect of Ce and La on the activity of CuO/ZSM-5 and MnO_x/ZSM-5 composites for elemental mercury removal at low temperature. *Fuel* **2017**, *194*, 115–122. [[CrossRef](#)]
32. Wu, J.; Liu, D.J.; Zhou, W.G.; Liu, Q.; Huang, Y. *High-Temperature H₂S Removal from IGCC Coarse Gas*; Springer Nature Singapore Pte Ltd.: Singapore, 2017.
33. Pfeifer, P.; Avnir, D. Chemistry in noninteger dimensions between two and three. I. Fractal theory of heterogeneous surfaces. *J. Chem. Phys.* **1983**, *79*, 3558–3565. [[CrossRef](#)]
34. Avnir, D.; Farin, D.; Pfeifer, P. Chemistry in noninteger dimensions between two and three. II. Fractal surface of adsorbents. *J. Chem. Phys.* **1983**, *78*, 3566–3571. [[CrossRef](#)]
35. Gil, A.; Cherkashinin, Y.G.; Korili, S.A. Fractal Dimension of a Pillared Montmorillonite from Nitrogen Adsorption at 77 K. *J. Chem. Eng. Data* **2004**, *49*, 639–641. [[CrossRef](#)]
36. Dąbrowski, A.; Podkościelny, P.; Hubicki, Z.; Barczak, M. Adsorption of phenolic compounds by activated carbon—a critical review. *Chemosphere* **2005**, *58*, 1049–1070. [[CrossRef](#)] [[PubMed](#)]
37. Sahouli, B.; Blacher, S.; Brouers, F. Applicability of the Fractal FHH Equation. *Langmuir* **1997**, *13*, 4391–4394. [[CrossRef](#)]
38. Wu, M.K. The roughness of aerosol particles: Surface fractal dimension measured using nitrogen adsorption. *Aerosol Sci. Technol.* **1996**, *25*, 392–398. [[CrossRef](#)]
39. Li, Y.; Long, C.; Tao, W.; Li, A.; Zhang, Q. Fractal dimensions of macroporous and hypercrosslinked polymeric adsorbents from nitrogen adsorption data. *J. Chem. Eng. Data* **2010**, *55*, 3147–3150. [[CrossRef](#)]

